Journal of Materials Science & Technology 73 (2021) 139–144

Contents lists available at ScienceDirect

Journal of Materials Science & Technology

journal homepage: www.jmst.org

Research Article

Mechanical, corrosion and magnetic behavior of a $CoFeMn_{1.2}NiGa_{0.8}$ high entropy alloy

Xiaoming Sun[a], Lingzhong Du[a,b,*], Hao Lan[a,b,*], Jingyi Cui[a], Liang Wang[c,d], Runguang Li[d], Zhiang Liu[e], Junpeng Liu[f], Weigang Zhang[a]

[a] State Key Laboratory of Multiphase Complex Systems, Institute of Process Engineering, Chinese Academy of Sciences, Beijing, 100190, China
[b] Innovation Academy for Green Manufacture, Chinese Academy of Sciences, Beijing, 100190, China
[c] School of Materials Science and Engineering, Beijing Institute of Technology, Beijing, 100081, China
[d] X-ray Science Division, Argonne National Laboratory, Argonne, Illinois, 60439, USA
[e] Experimental Teaching and Equipment Management Center, Qufu Normal University, Qufu, Shandong, 273165, China
[f] State Key Laboratory of Nonlinear Mechanics, Institute of Mechanics, Chinese Academy of Sciences, Beijing, 100190, China

ARTICLE INFO

Article history:
Received 21 June 2020
Received in revised form 21 July 2020
Accepted 9 August 2020
Available online 1 October 2020

Keywords:
High entropy alloys
High-energy X-ray diffraction
Compressive property
Corrosion resistance
Magnetic behavior

ABSTRACT

In this study, a magnetic high entropy alloy (HEA) of $CoFeMn_{1.2}NiGa_{0.8}$ was designed and prepared by arc melting in order to investigate its mechanical, corrosion and magnetic behavior. The results show that the alloy mainly possesses body-centered cubic (BCC) phase and face-centered cubic (FCC) phase. A high compressive strength of 1450 MPa, a strain of 18.5 % and a relatively low yield strength of 303 MPa in as-cast condition at room temperature can be achieved in the present alloy. In-situ high-energy X-ray diffraction technique was employed to reveal the deformation mechanism of $CoFeMn_{1.2}NiGa_{0.8}$ under uniaxial compression and the results show that the competition between BCC phase and FCC phase plays a significant role during the compressive process. The corrosion behavior of $CoFeMn_{1.2}NiGa_{0.8}$ was investigated in 3.5 wt% NaCl solution and it turned out that the alloy possessed good corrosion resistance. At last, the magnetic behavior of the $CoFeMn_{1.2}NiGa_{0.8}$ alloy was studied and it can present a high saturation magnetization of 94.5 emu/g and a coercivity of 26.4 Oe at 4 K. This work indicates that the present $CoFeMn_{1.2}NiGa_{0.8}$ HEA has promising applications as future magnetic functional materials.

© 2021 Published by Elsevier Ltd on behalf of The editorial office of Journal of Materials Science & Technology.

1. Introduction

Since Yeh et al. [1] introduced the novel multi-component alloy design concept of high entropy alloys (HEAs) in 2004, this new alloy system has aroused increasing attention during the past few years. Unlike the conventional alloys with one principal element, usually the HEAs can have five or more components in equimolar or near-equimolar fraction. It is reported that the solid-solution phase(s) of HEAs is(are) simple crystal structure(s), such as face-centered cubic (FCC), body-centered cubic (BCC), and/or hexagonal closed-pack (HCP) lattices [2]. In some reported film HEAs and small-size HEAs, they can also present an amorphous structure because of the low glass-forming ability [3]. Owing to their unique concentrated solid-solution structures, HEAs have distinguished properties, such as high strength [4], excellent fracture toughness [5], high fatigue resistance [6], good ductility [7], good wear and corrosion resistance [8], good thermal stability [9] and high electrical resistivity [10], which are also related to the four "core effects" in HEAs: high entropy of mixing, sluggish diffusion, severe lattice distortion and cocktail effects [1]. Although the above properties of HEAs play a significant role in the potential application, the magnetic performance of HEAs should also be developed since magnetic HEAs with high performance can be a good candidate as magnetic materials in the fields such as electric motors, magnetic shielding, hysteresis motor, signaling storage devices.

The ferromagnetic shape memory alloys (FSMAs) present potential application as magnetic-field-controlled actuator materials due to their fast response of magnetostrain across magnetic-field-induced phase transformation. So far, many FSMAs have been systematically studied, including Ni-(Co)-Mn-Ga [11], Fe-Mn-Ga [12], Ni-(Co)-Fe-Ga [13], etc. However, these magnetic Heusler alloys always show inherent brittleness, which seriously restricts

* Corresponding authors at: State Key Laboratory of Multiphase Complex Systems, Institute of Process Engineering, Chinese Academy of Sciences, Beijing, 100190, China.
E-mail addresses: lzdu@ipe.ac.cn (L. Du), hlan@ipe.ac.cn (H. Lan).

https://doi.org/10.1016/j.jmst.2020.08.062
1005-0302/© 2021 Published by Elsevier Ltd on behalf of The editorial office of Journal of Materials Science & Technology.

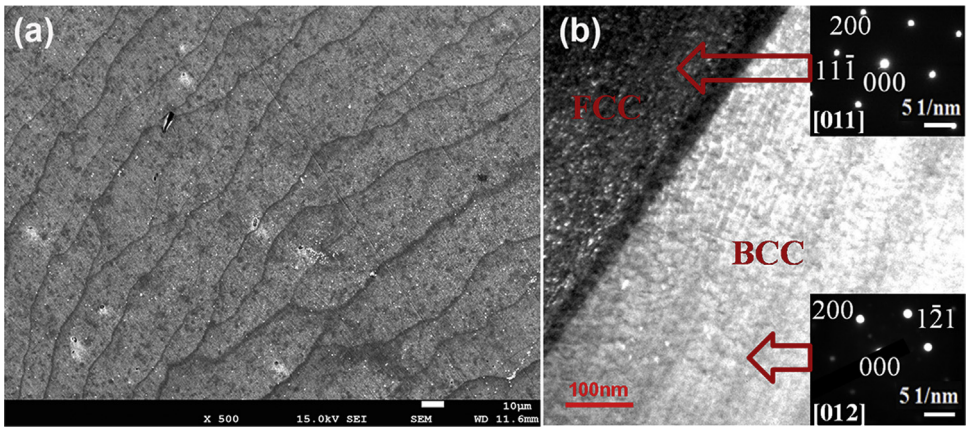

Fig. 1. (a) SEM micrograph and (b) TEM image with the corresponding SAED patterns of the $CoFeMn_{1.2}NiGa_{0.8}$ alloy.

their applications when the materials need to be processed into desired shapes for real devices during service [14]. Moreover, the corrosion resistance of many FSMAs should also be strengthened since the materials are usually used in complex environment [15,16]. As mentioned above, HEAs can show excellent mechanical properties and good corrosion resistance. Thus, combining the advantages of HEAs and FSMAs to search for alloys with potential magnetic-field-induced properties may be a viable option to obtain high-performance magnetic materials.

In this work, a new $CoFeMn_{1.2}NiGa_{0.8}$ high entropy alloy was carefully designed for the purpose of achieving a magnetic HEA material. The microstructure, mechanical, corrosion and magnetic properties of the present alloy were investigated in detail. This study may provide insight into how HEAs can be developed towards the magnetic applications.

2. Experimental

The ingot with nominal composition of $CoFeMn_{1.2}NiGa_{0.8}$ was prepared by repeated melting in an arc furnace under argon atmosphere. Raw elements with purity higher than 99.95 wt% were selected and additional 3 wt% Mn was added to alleviate the Mn evaporation during melting. The sample was re-melted five times at ~ 2273 K to ensure chemical homogeneity. The microstructure was characterized by scanning electron microscopy (SEM) (Zeiss Supra 55) (equipped with energy-dispersive (EDS) detector) and transmission electron microscopy (TEM, JEM-2100 F, JEOL, Japan). Compressive tests on samples with the size of $\Phi 2 \times 5$ mm^3 were conducted by using a mechanical testing machine (Instron-5966) equipped with a heating and cooling device with a rate of 10 K/min. The potentiodynamic polarization experiments were conducted on a CHI 660D electrochemical working station with a three-electrode measurement system implemented by using 3.5 wt% NaCl solution at 308 K. The $CoFeMn_{1.2}NiGa_{0.8}$ alloy or 304 stainless steel was regarded as the working electrode, with a platinum foil as the counter electrode and a saturated calomel electrode (SCE) as the reference electrode. The open current potential (OCP) was tested for 7200 s to make the potential stable before the potentiodynamic polarization test. After the polarization experiment, the samples were all cleaned by ultrasonic wash and then SEM experiment was performed on the observation of the morphology of the corroded surface. Magnetic measurements were performed by using a Physical Property Measurement System (PPMS, Quantum Design) and the magnetic hysteresis loops were measured at 4 K and 297 K with a variable magnetic field rate of 100 Oe/s. Differential scanning calorimetry (DSC, NETZSCH200F3) experiments were performed with a heating and cooling rate 10 K/min. In-situ synchrotron high-energy X-ray diffraction (HEXRD) experiments were carried out at the 11-ID-C beamline at the Advanced Photon Source of Argonne National Laboratory. A monochromatic X-ray beam with a wavelength of 0.1173 Å was used. The diffraction Debye rings were collected on a two-dimensional large area detector. The HEXRD images were processed by using the Fit2D image processing software.

Table 1
Chemical composition (at%) of the $CoFeMn_{1.2}NiGa_{0.8}$ alloy.

Elements	Co	Fe	Mn	Ni	Ga
Nominal	20	20	24	20	16
Present	19.34	18.99	24.32	20.16	17.19

3. Results and discussion

3.1. Microstructural and phase analysis

Fig. 1(a) shows the low magnified SEM image of the as-cast $CoFeMn_{1.2}NiGa_{0.8}$ alloy. It is clear that the present alloy is polycrystalline. One can see that the $CoFeMn_{1.2}NiGa_{0.8}$ alloy shows a columnar-grain morphology with the average grain size larger than 100 μm in the length direction; however, one cannot distinguish the potential FCC phase structure from the BCC phase structure from Fig. 1(a). The EDS analysis can be seen in Table 1. Fig. 1(b) shows the TEM image and the corresponding selected area electron diffraction (SAED) patterns for the $CoFeMn_{1.2}NiGa_{0.8}$ alloy. Interestingly, a sharp boundary was detected in the alloy. By identifying the electron diffraction patterns, our careful analysis shows that a FCC phase on the left side and a BCC phase on the right side can be confirmed in Fig. 1(b). As a result, the structures of the present alloy may mainly consist of FCC and BCC, which can further be confirmed in Fig. 2.

HEXRD experiment was employed to identify the primary phase structure of the as-cast $CoFeMn_{1.2}NiGa_{0.8}$ alloy, and the results are shown in Fig. 2.The HEXRD has high resolution, which ensures the accuracy of the crystal structure information. As shown in Fig. 2, the HEXRD patterns at 293 K can be well indexed according to the BCC structure with the lattice constant of 2.863 Å and the FCC structure with the lattice constant of 3.661 Å. This is consistent with the TEM results shown in Fig. 1(b). As a result, the present alloy mainly possesses BCC and FCC-based phase structure.

3.2. In-situ study of compressive properties

Fig. 3 shows the typical compressive stress-strain curves recorded for $CoFeMn_{1.2}NiGa_{0.8}$ at 113 K, 293 K, 523 K and 773

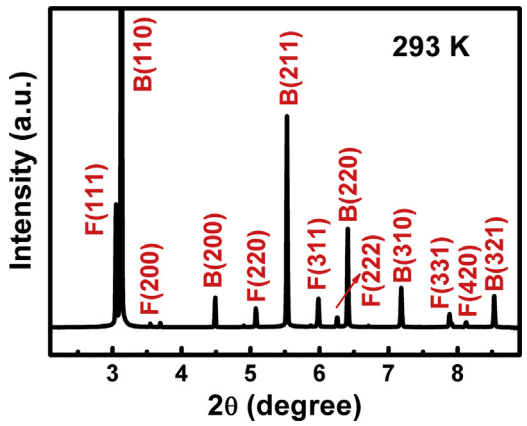

Fig. 2. One-D HEXRD profile of the $CoFeMn_{1.2}NiGa_{0.8}$ alloy at room temperature.

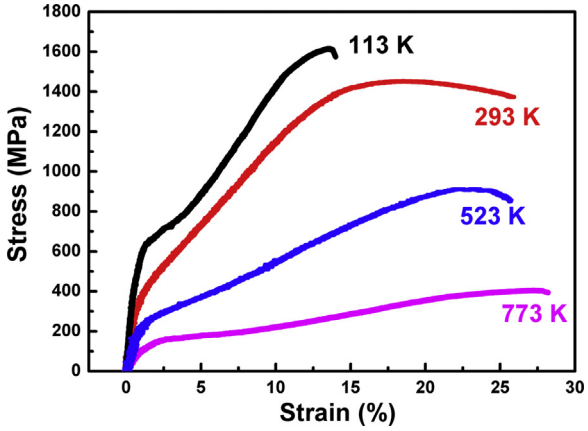

Fig. 3. The nominal uniaxial compression stress-strain curve of $CoFeMn_{1.2}NiGa_{0.8}$ at different temperatures.

K, respectively. One can see that at 293 K which is close to the room temperature, the compressive strength and strain of $CoFeMn_{1.2}NiGa_{0.8}$ are ~1450 MPa and ~18.5 %. Following the elastic deformation stage, work hardening associated with true plastic deformation (based on dislocation slip) occurs at 293 K. However, these two activities cannot be clearly and totally separated owing to the polycrystalline nature of the present alloy. For comparison, the compressive strength and strain of the present alloy at room temperature are much higher than that of the Ni(Fe)MnGa magnetic shape memory alloys [17,18], although they are a little lower than that of the CoCrFeMnNi high entropy alloy [19]. This may be caused by the different phase compositions and their contents in these alloys; different phases can bear different magnitudes of stress when the external stress is applied. The present $CoFeMn_{1.2}NiGa_{0.8}$ alloy possesses more FCC phase compared with Ni(Fe)MnGa magnetic shape memory alloys. The phase volume fractions of the BCC and FCC phases in the present HEA at room temperature have been roughly estimated to be ~ 84 % and ~ 16 %, respectively. Due to the coarse grains of the alloy and the limitation of experimental conditions, the volume fractions of the BCC and FCC phases during compressive process is not given here. The cooling rate during preparation or heat treatment determining the size of grains as well as some nanoparticles may also play an important role in the evaluation of mechanical properties for HEAs. Moreover, the present alloy demonstrates relatively low yield strength of 303 MPa at 293 K, which may show good cold working formability for application. As can be seen from Fig. 3, the increase in testing temperature leads to the decrease of both the compressive and the yield strength. At all tested temperatures, $CoFeMn_{1.2}NiGa_{0.8}$ maintains relatively high compression ductility and can all be strained to over 10 % reduction.

Table 2
Electrochemical parameters derived from polarization curves of $CoFeMn_{1.2}NiGa_{0.8}$ and 304 stainless steel in 3.5 wt% NaCl solution.

Alloys	E_{corr}(V_{SCE})	I_{corr}(A cm^{-2})	E_p(V_{SCE})
$CoFeMn_{1.2}NiGa_{0.8}$	−0.416	1.11×10^{-3}	0.79
304 stainless steel	−0.489	1.37×10^{-3}	0.22

The evolution of the one-dimensional (1D) HEXRD patterns (obtained by azimuthal integration of the 2θ range from 3° to 3.2° and 5.35° to 5.65°) during applying compressive stress is shown in Fig. 4(a). One can see that no new peaks can be detected near the F(111), B(110) and B(211) diffraction peaks during increasing the compressive stress, though the B(110) and B(211) diffraction peaks exhibite an increasing-intensity and a shift towards the higher 2θ values while the F(111) diffraction peak keeps almost stable under external stress. Lattice strain-stress curves for F{111}, B{110} and B{211} planes under different compressive stresses are presented in Fig. 4(b). The structure evolution can be clearly understood from the change in lattice strains ε_{hkl} ($\varepsilon_{hkl} = (d_{hkl}-d_0)/d_0$), where d_0 and d_{hkl} are the interplanar spacings for different (hkl) crystalline planes before and after applying an external stress. As shown in Fig. 4(b), the lattice strains of F{111}, B{110} and B{211} planes increase slowly at first (stress lower than 400 MPa) and then present a sharp increase (stress between 400 MPa and 1200 MPa) and then keep stable at last (stress higher than 1200 MPa). The slopes of the lattice strain curves of the B{110} and B{211} planes are obviously higher than that of F{111}. In addition, the lattice strains of the B{110} and B{211} planes during plastic deformation stage are much higher than that of the F{111}, indicating that the BCC phase bore much more stress than the FCC phase during this process. The evolution of the full width at half maximum (FWHM) for the F(111), B(110) and B(211) diffraction peaks of $CoFeMn_{1.2}NiGa_{0.8}$ which can present more information of deformation mechanisms, is shown in Fig. 4(c). When the stress is lower than 400 MPa, the FWHM of the F(111) diffraction peak almost keeps stable while FWHMs of B(110) and B(211) diffraction peaks increase slightly. Similar to the lattice strains shown in Fig. 4(b), one can see that FWHMs of B(110) and B(211) diffraction peaks increase rapidly and faster than that of the F(111) diffraction peak when the applied stress exceeds 400 MPa. The differences in the increase trend of FWHMs between BCC and FCC phases, on the one hand, may be caused by the coherent scattering volumes' decreasing speed in different phases. On the other hand, during increasing the stress the crystal defects and micro-stresses may change, leading to further inhomogeneous strain in different phases. Overall, Fig. 4 clearly accounts for the rough competition trend between BCC phase and FCC phase during the compressive process.

3.3. Corrosion behavior

Excellent corrosion resistance is crucial for application in HEAs [2]. Fig. 5 presents the corrosion behavior of $CoFeMn_{1.2}NiGa_{0.8}$ after testing in the 3.5 wt% NaCl solution, where a 304 stainless steel was also investigated for comparison. For clarify, the electrochemical parameters are displayed in Table 2. As shown in Fig. 5(a), the corrosion potential E_{corr} for $CoFeMn_{1.2}NiGa_{0.8}$ (-0.416 V) is higher than that of 304 stainless steel (-0.489 V), while the corrosion density I_{corr} of $CoFeMn_{1.2}NiGa_{0.8}$ is smaller. Besides, one can see from Fig. 5(a) that $CoFeMn_{1.2}NiGa_{0.8}$ presents better critical pitting potential E_p than that of the 304 stainless steel, indicating that the protective passive film started to pit earlier on the surface of the 304 stainless steel than on $CoFeMn_{1.2}NiGa_{0.8}$. The above observations demonstrate that the passive $CoFeMn_{1.2}NiGa_{0.8}$

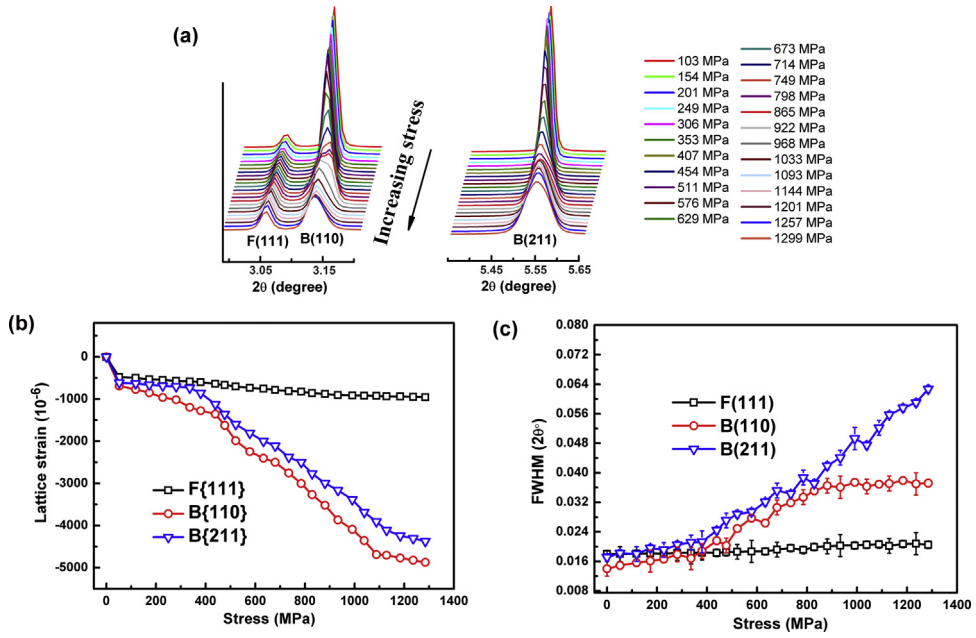

Fig. 4. (a) 1-D HE-XRD profiles evolution of F(111), B(110) and B(211) under stress by integrating the 2-D diffraction patterns of the 2θ range from 3° to 3.2° and 5.35° to 5.65°. (b) Response of lattice strains to compressive stress of the F{111}, B{110} and B{211} phases in $CoFeMn_{1.2}NiGa_{0.8}$. (c) The change in FWHMs for F(111), B(110) and B(211) peaks as a function of uniaxial compression in $CoFeMn_{1.2}NiGa_{0.8}$.

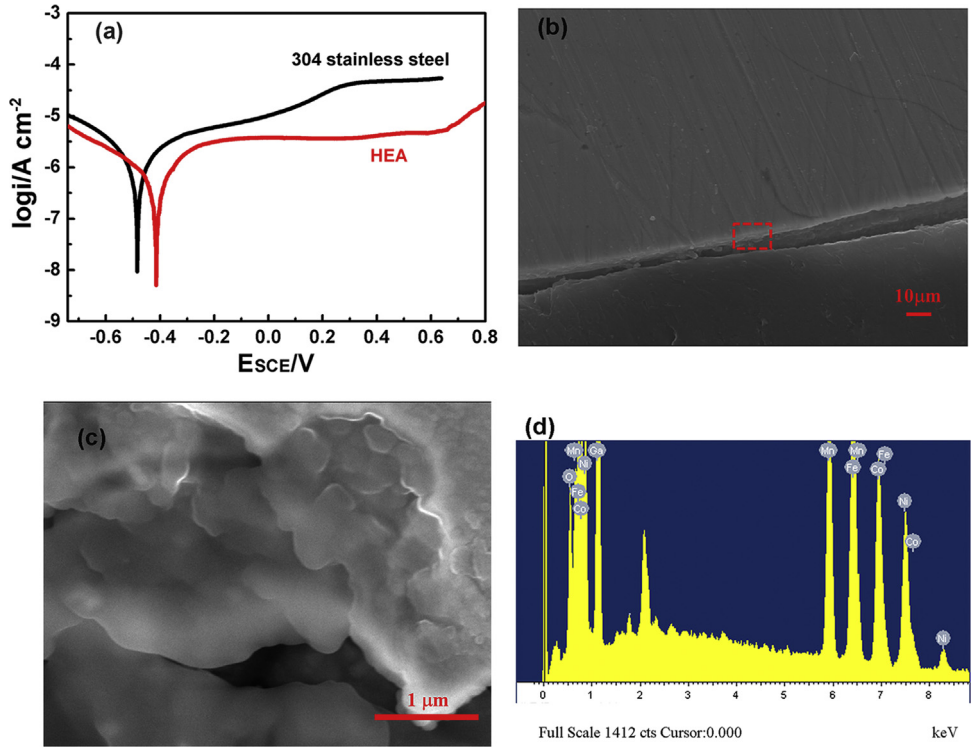

Fig. 5. (a) Corrosion tests of the $CoFeMn_{1.2}NiGa_{0.8}$ alloy and steel in 3.5 wt% NaCl solution at 308 K. (b) SEM micrograph of $CoFeMn_{1.2}NiGa_{0.8}$ after corrosion. (c) Enlarged views of filed in the frame in (b). (d) EDS analysis of (c).

has better resistance to the surface corrosion. It is reported that the elements Co and Ni in HEAs have excellent corrosion resistance, and they can easily form protective layers on the surface of materials [20–22]. This is further confirmed by our SEM analysis. The SEM micrographs of $CoFeMn_{1.2}NiGa_{0.8}$ after corrosion in 3.5 wt% NaCl solution are shown in Fig. 5(b) and (c). As can be seen, the formation of some layer-like morphology appeared on the surface and on the particles of corroded $CoFeMn_{1.2}NiGa_{0.8}$. These layers result from the oxide of Ni and Co to prevent the material from further corrosion, as indicated by the oxygen peak in the EDS results of Fig. 5(d). In addition to the existence of Ni and Co elements, the homogeneously distributed elements (as shown in Table 1) forming the protective layer also play significant roles.

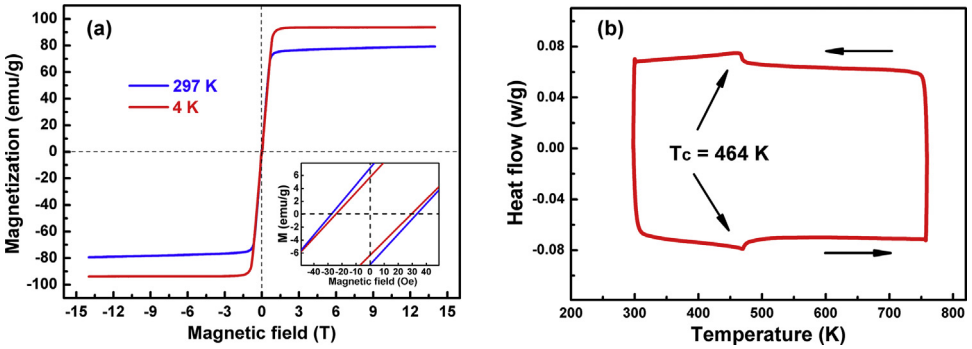

Fig. 6. (a) Magnetic hysteresis loops of $CoFeMn_{1.2}NiGa_{0.8}$ at 297 K and 4 K. The inset of (a) is the coercivity of $CoFeMn_{1.2}NiGa_{0.8}$. (b) The DSC curve of $CoFeMn_{1.2}NiGa_{0.8}$ recorded between 300 K and 750 K.

3.4. Magnetic characteristics

The typical magnetic hysteresis loops of $CoFeMn_{1.2}NiGa_{0.8}$ at 297 K and 4 K are shown in Fig. 6(a). One can see that the magnetization processes of $CoFeMn_{1.2}NiGa_{0.8}$ at 297 K and 4 K present almost the same trend before saturation, which means it has similar magnetic susceptibility behavior between 4 K and 297 K. Significantly, one should notice that the saturation magnetization (M_s) of $CoFeMn_{1.2}NiGa_{0.8}$ can reach 79.2 emu/g at 297 K and 94.5 emu/g at 4 K, respectively. It is reported that when the temperature is much lower than the Curie temperature (obtained from Fig. 6(b)), the atoms' thermal vibration cannot affect the magnetic ordering. When the temperature increases, the atoms' thermal vibration behavior will be exacerbated, leading to the atomic magnetic ordering decreased and further resulting in a decrease of the saturation magnetization [23]. Overall, the high saturation magnetization in the present alloy has exceeded most of other HEAs [24–28], and can even compete with that of many FSMAs [29–32]. As can be seen from the inset of Fig. 6(a), the coercivity (H_c) of $CoFeMn_{1.2}NiGa_{0.8}$ is about 31.1 Oe at 297 K. When the temperature decreases to 4 K, the coercivity slightly decreases to 26.4 Oe. Fortunately, the present $CoFeMn_{1.2}NiGa_{0.8}$ alloy distributes in a semi-hard magnetic region for future application [33,34], which provides a possibility to use this materials in the field such as rotor or storage elements of hysteresis motor. Fig. 6(b) shows DSC curves of $CoFeMn_{1.2}NiGa_{0.8}$. No martensitic transformation behavior can be observed between 300 K and 750 K during heating and cooling and the Curie temperature is determined to be 464 K.

For NiMnGa-based FSMAs, replacing Ni by Fe or Co can change the Mn-Mn coupling and greatly increase the magnetization of austenite phase. The replacement of Ni by Fe may stabilize or reduce the Curie temperature in certain Ni-Mn-Ga alloys [35,36], while replacing Ni by Co may significantly increase the Curie temperature [37]. As a result, it can be optional when tuning the M_s or changing the Curie temperature windows in a CoFeMnNiGa magnetic high entropy alloy system. Besides, from a phase composition standpoint, usually the FCC phase shows a higher M_s than that of BCC phase [7]. As for H_c, the microstructure such as grain size and grain orientation can have large effects. When considering the factor of grain size, H_c can be determined by the following equation [35]:

$$H_C \approx 3\sqrt{\frac{\kappa_B T_C}{\alpha M_S}}\sqrt{\frac{1}{D}} \quad (1)$$

where κ_B is the Boltzmann constant, D the average grain size, and α is the lattice constant. According to Eq. (1), for $CoFeMn_{1.2}NiGa_{0.8}$, H_c is inversely proportional to $M_s^{1/2}$. This is in accordance with our result since H_c at 297 K is higher than that at 4 K. Our further investigation shows that the magnetic-field-induced strain in the present alloy can be up to 32.1 × 10^{-6} under the magnetic field of 1 T (which is not shown here). This strain value is not in magnitude with that in the FSMA NiMnGa showing martensitic transformation, which should be further improved in the following work towards the direction of ferromagnetic high entropy shape memory alloys. As mentioned above, the present $CoFeMn_{1.2}NiGa_{0.8}$ alloy belongs to a semi-hard magnetic material. Fig. 7 schematically displays the magnetic properties of magnetization and coercivity values for some reported HEAs distributing in the semi-hard magnetic region [38–46]. As can be seen, the alloy of the current work, $CoFeMn_{1.2}NiGa_{0.8}$, has reasonably good coercivity which is pretty close to the soft magnetic region and relatively high magnetization value compared with that of the HEAs reported before. Consequently, the present alloy can be applied as semi hard magnetic HEAs with great potentialities, particularly in the field of magnetic materials used under complex environments such as cryogenic temperature, heavy load, salt spray corrosion.

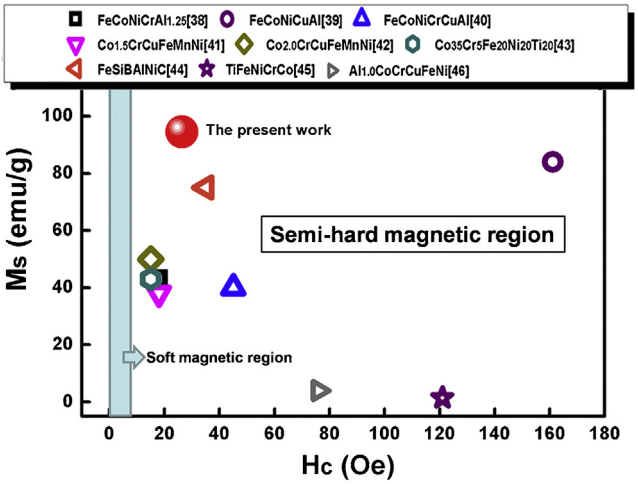

Fig. 7. Scatter plot of the magnetic properties for $CoFeMn_{1.2}NiGa_{0.8}$ and some reported magnetic HEAs.

4. Conclusion

In summary, a new $CoFeMn_{1.2}NiGa_{0.8}$ high entropy alloy has been successfully developed. The microstructure, mechanical, corrosion and magnetic properties were investigated. The results show that the $CoFeMn_{1.2}NiGa_{0.8}$ alloy mainly composes of BCC matrix and FCC phase, and can achieve a compressive strength of ~1450 MPa, a strain of ~18.5 % and a yield strength of 303 MPa in the as-cast condition at room temperature. The in-situ high-energy X-ray diffraction experiments were employed to reveal the deforma-

tion mechanism of $CoFeMn_{1.2}NiGa_{0.8}$ under uniaxial compression and it indicates that the competition between BCC phase and FCC phase greatly affects the compressive process. The present alloy is proved to present good corrosion resistance. Moreover, the magnetic investigation shows that the present alloy belonging to semi-hard magnetic materials possesses a high saturation magnetization of 94.5 emu/g and a coercivity of 26.4 Oe at 4 K and a Curie temperature of 464 K. This study may provide an in-depth understanding of elastic deformation mechanism for HEAs and shed light on the design of HEAs especially for magnetic applications.

Acknowledgements

We gratefully acknowledge support from the National Key Research and Development Program of China (No. 2018YFC1902401) and National Natural Science Foundation of China (No. 51671180). This work is also supported by Key Deployment Projects of the Chinese Academy of Sciences (ZDRW-CN-2019-01) and Projects of the Innovation Academy for Green Manufacture, Chinese Academy of Sciences (IAGM 2020DB04).

References

[1] J.W. Yeh, S.K. Chen, S.J. Lin, J.Y. Gan, T.S. Chin, T.T. Shun, C.H. Tsau, S.Y. Chang, Adv. Eng. Mater. 6 (2004) 299–303.
[2] Y. Zhang, T.T. Zuo, Z. Tang, M.C. Gao, K.A. Dahmen, P.K. Liaw, Z.P. Lu, Prog. Mater. Sci. 61 (2014) 1–93.
[3] S.F. Zhao, Y. Shao, X. Liu, N. Chen, H.Y. Ding, K.F. Yao, Mater. Des. 87 (2015) 625–631.
[4] S.H. Li, D.Y. Cong, X.M. Sun, Y. Zhang, Z. Chen, Z.H. Nie, R.G. Li, F.Q. Li, Y. Ren, Y.D. Wang, Mater. Res. Lett. 7 (2019) 482–489.
[5] B. Gludovatz, A. Hohenwarter, D. Catoor, E.H. Chang, E.P. George, R.O. Ritchie, Science 345 (2014) 1153–1158.
[6] A.G. Wang, X.H. An, J. Gu, X.G. Wang, L.L. Li, W.L. Li, M. Song, Q.Q. Duan, Z.F. Zhang, X.Z. Liao, J. Mater. Sci. Technol. 39 (2020) 1–6.
[7] Z.F. Lei, X.J. Liu, Y. Wu, H. Wang, S.H. Jiang, S.D. Wang, X.D. Hui, Y.D. Wu, B. Gault, P. Kontis, D. Raabe, Q.H. Zhang, H.W. Chen, H.T. Wang, J.B. Liu, K. An, Q.S. Zeng, T.G. Nieh, Z.P. Lu, Nature 563 (2018) 546–550.
[8] M.H. Chuang, M.H. Tsai, W.R. Wang, S.J. Lin, J.W. Yeh, Acta Mater. 59 (2011) 6308–6317.
[9] W.R. Wang, W.L. Wang, J.W. Yeh, J. Alloys Compd. 589 (2014) 143–152.
[10] C.D. Zhao, J.S. Li, Y.X. He, J.X. Wang, W.Y. Wang, H.C. Kou, J. Wang,J. Alloys Compd. 820 (2020), 153407.
[11] S.Y. Yu, Z.X. Cao, L. Ma, G.D. Liu, J.L. Chen, G.H. Wu,Appl. Phys. Lett. 91 (2007), 102507.
[12] X.M. Sun, D.Y. Cong, Y. Ren, K.-D. Liss, D.E. Brown, Z.Y. Ma, S.J. Hao, W.X. Xia, Z. Chen, L. Ma, X.G. Zhao, Z.B. He, J. Liu, R.G. Li, Y.D. Wang, Acta Mater. 183 (2020) 11–23.
[13] J. Liu, N. Scheerbaum, D. Hinz, O. Gutfleisch, Acta Mater. 56 (2008) 3177–3186.
[14] D.Y. Cong, L. Huang, V. Hardy, D. Bourgault, X.M. Sun, Z.H. Nie, M.G. Wang, Y. Ren, P. Entel, Y.D. Wang, Acta Mater. 146 (2018) 142–151.
[15] X.W. Liu, O. Söderberg, Y.Y. Ge, A. Sozinov, V.K. Lindroos, Mater. Sci. Forum 394–395 (2002) 565–568.
[16] A. Gebert, S. Roth, S. Oswald, Corros. Sci. 51 (2009) 1163–1171.
[17] A.A. Likhachev, K. Ullakko, Phys. Lett. A 275 (2000) 142–151.
[18] X.M. Sun, D.Y. Cong, Y. Ren, D.E. Brown, R.G. Li, S.H. Li, Z. Yang, W.X. Xiong, Z.H. Nie, L. Wang, Y.D. Wang,Appl. Phys. Lett. 113 (2018), 041903.
[19] Ł. Rogal, D. Kalita, A. Tarasek, P. Bobrowski, F. Czerwinski, J. Alloys Compd. 708 (2017) 344–352.
[20] L.B. Gao, W.B. Liao, H.T. Zhang, J.U. Surjadi, D. Sun, Y. Lu, Coatings 7 (2017) 156.
[21] R.K. Mishra, P.P. Sahay, R.R. Shahi, J. Mater. Sci. 54 (2019) 4433–4443.
[22] Y.Q. Jiang, J. Li, Y.F. Juan, Z.J. Lu, W.L. Jia, J. Alloys Compd. 775 (2019) 1–14.
[23] T.T. Zuo, M.C. Gao, L.Z. Ouyang, X. Yang, Y.Q. Cheng, R. Feng, S.Y. Chen, P.K. Liaw, J.A. Hawk, Y. Zhang, Acta Mater. 13 (2017) 10–18.
[24] F. Alijani, M. Reihanian, Kh. Gheisari, J. Alloys Compd. 773 (2019) 623–630.
[25] R.K. Mishra, R.R. Shahi, J. Magn. Magn. Mater. 442 (2017) 218–223.
[26] R.F. Zhao, B. Ren, G.P. Zhang, X.L. Zhong, B. Cai, J.J. Zhang, J. Magn. Magn. Mater. 468 (2018) 14–24.
[27] J. Xu, C.Y. Shang, W.J. Ge, H.L. Jia, P.K. Liaw, Y. Wang, Adv. Powder Technol. 27 (2016) 1418–1426.
[28] M.S. Lucas, L. Mauger, J.A. Munoz, Y.M. Xiao, A.O. Sheets, S.L. Semiatin, J. Horwath, Z. Turgut,J. Appl. Phys. 109 (2011), 07E307.
[29] K. Ullakko, J.K. Huang, C. Kantner, R.C. OHandley, V.V. Kokorin, Appl. Phys. Lett. 69 (1996) 1966–1968.
[30] D.Y. Cong, S. Roth, L. Schultz, Acta Mater. 60 (2012) 5335–5351.
[31] R. Kainuma, Y. Imano, W. Ito, Y. Sutou, H. Morito, S. Okamoto, O. Kitakami, K. Oikawa, A. Fujita, T. Kanomata, K. Ishida, Nature 439 (2006) 957–960.
[32] D.E. Soto-Parra, X. Moya, L. Mañosa, A. Planes, H. Flores-Zúñiga, F. Alvarado-Hernández, R.A. Ochoa-Gamboa, J.A. Matutes-Aquino, D. Ríos-Jara, Philos. Mag. A 90 (2010) 2771–2792.
[33] J. He, L. Zhou, D.L. Zhao, X.L. Wang, J. Mater. Res. 24 (2009) 1607–1610.
[34] R.F. Zhao, B. Ren, G.P. Zhang, Z.X. Liu, B. Cai, J.J. Zhang,J. Magn. Magn. Mater. 491 (2019), 165574.
[35] T.T. Zuo, M. Zhang, P.K. Liaw, Y. Zhang, Intermetallics 100 (2018) 1–8.
[36] S.Y. Yu, S.S. Yan, S.S. Kang, X.D. Tang, J.F. Qian, J.L. Chen, G.H. Wu, Scripta Mater. 65 (2011) 9–12.
[37] A.A. Cherechukin, T. Takagi, J. Appl. Phys. 1740 (2004) 95.
[38] Y.F. Kao, S.K. Chen, T.J. Chen, P.C. Chu, J.W. Yeh, S.J. Lin, J. Alloys Compd. 509 (2011) 1061–1067.
[39] R. Kulkarni, B.S. Murty, V. Srinivas, J. Alloys Compd. 746 (2018) 194–199.
[40] S. Singh, N. Wanderka, K. Kiefer, U. Glatzel, J. Banhart, Acta Mater. 59 (2011) 182–190.
[41] Z.Q. Fu, B.E. Macdonald, A.D. Dupuy, X. Wang, T.C. Monson, R.E. Delaney, C.J. Pearce, K. Hu, Z.F. Jiang, Y.Z. Zhou, J.M. Schoenung, W.P. Chen, E.J. Lavernia, Appl. Mater. Today 15 (2019) 590–598.
[42] J. Wang, Z. Zhang, J. Xu, Y. Wang, J. Magn. Magn. Mater. 355 (2014) 58–64.
[43] K. Yamauchi, Y. Yoshizawa, Mater. Sci. Eng. A 133 (1991) 180–183.
[44] X.X. Zhu, X. Zhou, S.S. Yu, C.C. Wei, J. Xu, Y. Wang, J. Magn. Magn. Mater. 430 (2017) 59–64.
[45] M.G. Poletti, G. Fiore, B.A. Szost, L. Battezzati, J. Alloys Compd. 620 (2015) 283–288.
[46] A.Q. Mao, P.P. Ding, F. Quan, T.C. Zhang, X.Q. Ran, Y.B. Li, X. Jin, X.L. Gu, J. Alloys Compd. 735 (2018) 1167–1175.